ADVANCED MATERIALS
www.advmat.de

Suppressed Defects by Functional Thermally Cross-Linked Fullerene for High-Efficiency Tin-Lead Perovskite Solar Cells

Jinbo Zhao, Zhenhuang Su, Jorge Pascual, Hongzhuo Wu, Haibin Wang, Mahmoud H. Aldamasy, Zhengji Zhou, Chenyue Wang, Guixiang Li, Zhe Li,* Xingyu Gao, Chain-Shu Hsu,* and Meng Li**

Mixed tin-lead (Sn-Pb) perovskites have attracted the attention of the community due to their narrow bandgap, ideal for photovoltaic applications, especially tandem solar cells. However, the oxidation and rapid crystallization of Sn^{2+} and the interfacial traps hinder their development. Here, cross-linkable [6,6]-phenyl-C_{61}-butyric styryl dendron ester (C-PCBSD) is introduced during the quenching step of perovskite thin film processing to suppress the generation of surface defects at the electron transport layer interface and improve the bulk crystallinity. The C-PCBSD has strong coordination ability with Sn^{2+} and Pb^{2+} perovskite precursors, which retards the crystallization process, suppresses the oxidation of Sn^{2+}, and improves the perovskite bulk and surface crystallinity, yielding films with reduced nonradiative recombination and enhanced interface charge extraction. Besides, the C-PCBSD network deposited on the perovskite surface displays superior hydrophobicity and oxygen resistance. Consequently, the devices with C-PCBSD obtain PCEs of up to 23.4% and retained 97% of initial efficiency after 2000 h of storage in a N_2 atmosphere.

1. Introduction

Metal halide perovskite solar cells (PSCs) have attracted the photovoltaic community´s attention due to their superior optical and electrical performance, such as tunable bandgap, high carrier transport mobilities, long electron–hole pair diffusion lengths, and small exciton binding energies. As a result, the power conversion efficiency (PCE) of PSCs surged from 3.8% to 26.15% in around one decade.[1–5] To overcome the Shockley–Queisser limit and further enhance the solar cell efficiency, tandem solar cells have been proposed with theoretical potential of achieving PCEs over 40%. Particularly, all-perovskite tandem solar cells require a narrow bandgap absorber of 1.2 eV. However, traditional high-efficiency lead-based materials show bandgaps wider than 1.45 eV. Meanwhile,

J. Zhao, H. Wu, Z. Zhou, M. Li
Key Lab for Special Functional Materials of Ministry of Education
National & Local Joint Engineering Research Center for High-Efficiency Display and Lighting Technology
School of Nanoscience and Materials Engineering
and Collaborative Innovation Center of Nano Functional Materials and Applications
Henan University
Kaifeng 475004, P. R. China
E-mail: mengli@henu.edu.cn

Z. Su, C. Wang, X. Gao
Shanghai Synchrotron Radiation Facility (SSRF)
Shanghai Advanced Research Institute
Chinese Academy of Sciences
239 Zhangheng Road, Shanghai 201204, P. R. China

The ORCID identification number(s) for the author(s) of this article can be found under https://doi.org/10.1002/adma.202406246

DOI: 10.1002/adma.202406246

J. Pascual
POLYMAT
University of the Basque Country UPV/EHU
Donostia-San Sebastián 20018, Spain

H. Wang
Institute of Advanced Ceramics, Henan Academy of Sciences
Zhengzhou 450046, China
E-mail: HaibinWang@hnas.ac.cn

M. H. Aldamasy, G. Li
Helmholtz-Zentrum Berlin für Materialien und Energie GmbH
Hahn-Meitner-Platz 1, 14109 Berlin, Germany

Z. Li
School of Engineering and Materials Science (SEMS)
Queen Mary University of London
London E1 4NS, UK
E-mail: zhe.li@qmul.ac.uk

C.-S. Hsu
Department of Applied Chemistry and Center for Emergent Functional Matter Science
National Yang Ming Chiao Tung University
Hsinchu 300093, Taiwan
E-mail: cshsu@nycu.edu.tw

mixed tin-lead-based (Sn-Pb) perovskites have a narrow bandgap of around 1.2 eV, making them ideal for this purpose. Thus, developing high-quality mixed Sn-Pb perovskites is a promising path to achieve high efficiency all-perovskite tandem solar cells.

Defect generation during the solution processing of the polycrystalline films is largely responsible to limitations in performance.[6] In particular, grain surfaces of metal halide perovskite (film interfaces and grain boundaries) exhibit trap densities several orders of magnitude higher than within the grain.[7–9] These defects represent nonradiative recombination centers and decrease the photogenerated carrier concentration. These recombination losses reduce the quasi-Fermi level splitting, decreasing the open-circuit voltage (V_{OC}).[10–12] Thus, reducing the grain surface defects is necessary to obtain high-performance PSCs.

This defect generation is of particular concern for Sn-containing perovskites due to their intrinsic chemical characteristics. The tendency of Sn^{2+} species to oxidize to Sn^{4+} upon oxygen exposure leads to self-p-doping in perovskite materials. In addition, the higher Lewis acidity of Sn^{2+} compared to Pb^{2+} is an important factor accelerating the crystallization dynamics, promoting defects formation and low-quality microstructure perovskite film.[13,14] The Sn vacancies and deep-level traps, including uncoordinated Pb^{2+}, are usually generated at the perovskite/electron transporting layer (ETL) interface.[15–17] Meanwhile, traditional ETLs such as C_{60} cause a high degree of energy disorder due to molecular aggregation, further aggravating the generation of deep-level traps.[18,19] Thus, optimizing the perovskite/ETL interface to decrease interface defects, enhance interface crystallization, and achieve a uniform distribution of electron transport materials is crucial to improve device performance.

In this work, we introduce thermally cross-linked fullerene derivative PCBSD to improve the top interface of the perovskite layer and optimize the perovskite/ETL interface. The affinity of the C═O bond of C-PCBSD with Sn^{2+} and Pb^{2+} perovskite components has critical benefits for the solar cell performance. The coordination to metal cations effectively retards the crystallization process of precursor materials into perovskite, improve the perovskite crystallinity as described by in situ grazing-incidence wide-angle X-ray scattering (GIWAXS). Furthermore, characterization reveals the passivation of deep- and shallow-level defects under the synergistic effect of cross-linkable fullerene on bulk and surface defects. Finally, the network structure of C-PCBSD can effectively prevent air invasion and enhance the water-oxygen stability of Sn^{2+}. Consequently, the resulting C-PCBSD-modified devices with improved thin film quality show efficiencies of up to 23.4%. They maintain 97% of their initial power conversion efficiency (PCE) after 2000 h in a nitrogen atmosphere, and 96% after 1000 h with intermittent exposure to air. This work highlighting the benefits of functional cross-linked networks for antisolvent engineering realizing efficient and stable tin-lead PSCs.

2. Result and Discussion

To investigate the effect of C-PCBSD on mixed tin-lead perovskite films ($Cs_{0.1}FA_{0.6}MA_{0.3}Sn_{0.5}Pb_{0.5}I_3$), we dissolved the C-PCBSD in chlorobenzene and dripped it on the perovskite film during film formation. C-PCBSD was introduced into CB as an antisolvent not only to control the nucleation and crystal growth of the perovskite but also to reduce defect density and enhance charge collection. **Figure 1** shows the device structure, the chemical structure of C-PCBSD, and the working mechanism at a molecular level of the surface modification approach. The characteristics of C-PCBSD are as follows: 1) Fullerene Adduct with Styrene Groups: C-PCBSD contains styrene groups that increase van der Waals interactions in the solid state, leading to better film formation and stability. 2) Thermal Cross-Linking: The terminal styrene functional groups in C-PCBSD tend to react and form bonds with adjacent molecules under thermal activation without any initiator. This cross-linking process helps to stabilize the perovskite film and reduce defect states. 3) Solvent and Water Resistance: C-PCBSD exhibits high solvent and water-resistant properties, which enhance the environmental stability of the perovskite film. 4) Strong Coordination Ability: C-PCBSD has a strong coordination ability with Sn^{2+} and Pb^{2+} in perovskite precursors. This coordination retards the crystallization rate and suppresses the oxidation of Sn^{2+}, resulting in films with reduced nonradiative recombination and enhanced interface charge extraction. 5) Hydrophobic and Oxygen Resistance: The network structure of C-PCBSD deposited on the perovskite surface displays superior hydrophobicity and oxygen resistance.[20]

As shown in Figure 1a, PSCs based on a structure of fluorine doped tin-oxide (FTO)/Poly [3,4-ethylenedioxythiophene]:poly[styrene sulfonate] (PEDOT:PSS)/perovskite/C_{60}/Bphen/Ag are fabricated. During perovskite film annealing, the C-PCBSD tends to leak into the film and cross-link in a network at the grain boundaries and a thin layer on the surface through its olefinic branches.[21] The cross-linkage mechanism inside the film and its improved protecting ability is shown in Figure 1b–d; and Figure S1 (Supporting Information).

To investigate the molecular interaction between C-PCBSD and perovskite material, we carried out Fourier-transform infrared spectroscopy (FTIR) characterization. As shown in Figure 1e, the FTIR spectra show the change of C-PCBSD bands when deposited as a layer or on the perovskite film. The stretching vibration peak of the C═O bond of C-PCBSD located at 1735 shifted to 1712 cm^{-1} when deposited on perovskite films. This shift can be attributed to the C═O coordination bonds with undercoordinated Pb^{2+} and Sn^{2+} through Lewis acid-base interactions and the suppression of the Sn vacancies and uncoordinated Pb^{2+}.[22–24] The interaction between the C-PCBSD and the perovskite absorber was further confirmed by X-ray photoelectron spectroscopy (XPS). As shown in Figure 1f, the XPS peaks of Pb for the treated perovskite film appear at 142.6 and 137.7 eV, respectively, corresponding to Pb $4f_{5/2}$ and Pb $4f_{7/2}$, shifting 0.3 eV toward lower binding energy compared with the peaks of the control film. The Sn peaks for the treated perovskite film appear at 495.6 and 487.2 eV, corresponding to Sn $3d_{3/2}$ and Sn $3d_{5/2}$, respectively. In the same line as for Pb, we observe a shift of 0.4 eV toward lower binding energy compared to the control film (Figure S2, Supporting Information). This is attributed to the coordination of C═O and Pb^{2+}, Sn^{2+}, which control the crystallization process and passivates the defects at the grain boundaries and surfaces as shown in Figure 1d.[25]

The Sn-Pb perovskite films are investigated by atomic force microscopy (AFM) and scanning electron microscopy (SEM) to explore the effect of C-PCBSD on the microstructure quality of the perovskite film. **Figure 2**a,b shows the control film has more

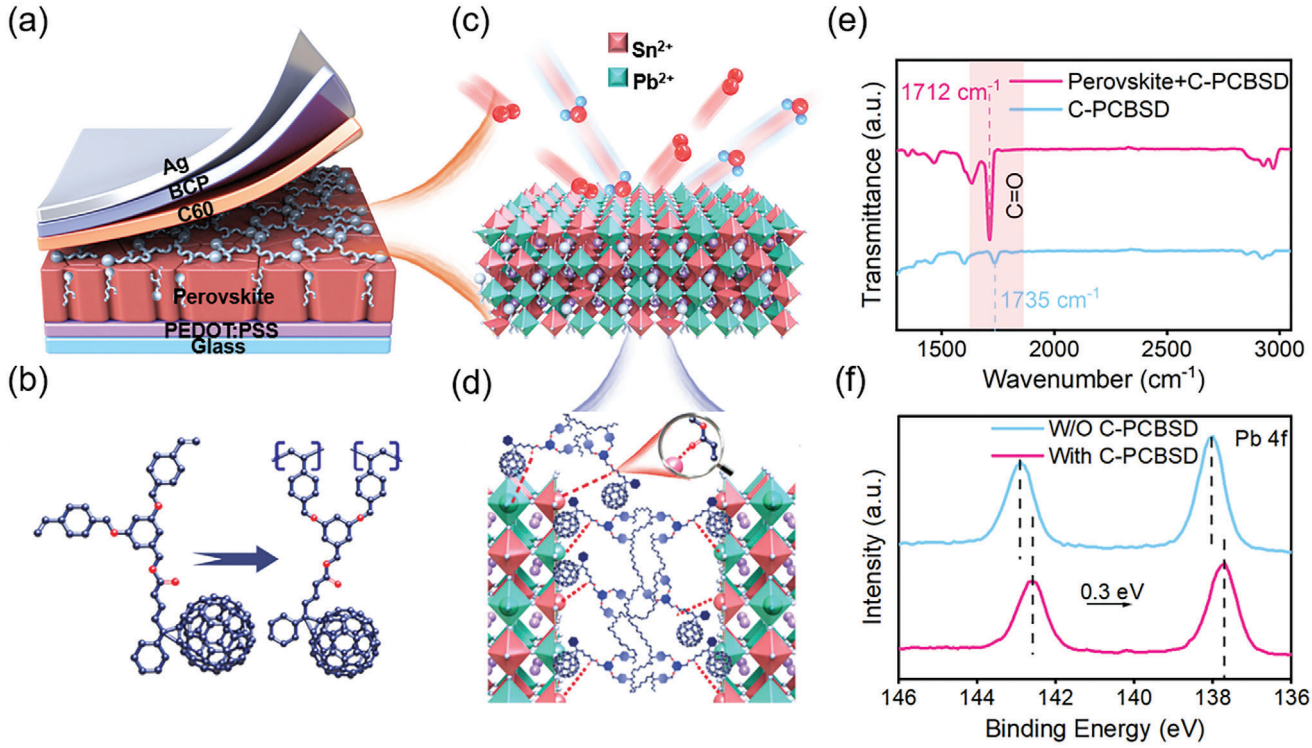

Figure 1. Schematic diagram of a) device structure of Sn-Pb PSCs treated with C-PCBSD. b) Cross-linking mechanism of C-PCBSD. c) Perovskite lattice protected from water and oxygen and d) illustration of internal cross-linked C-PCBSD. e) FTIR spectra of C-PCBSD and perovskite film treated with C-PCBSD. f) XPS chart of Pb 4f of control and C-PCBSD-treated perovskite films.

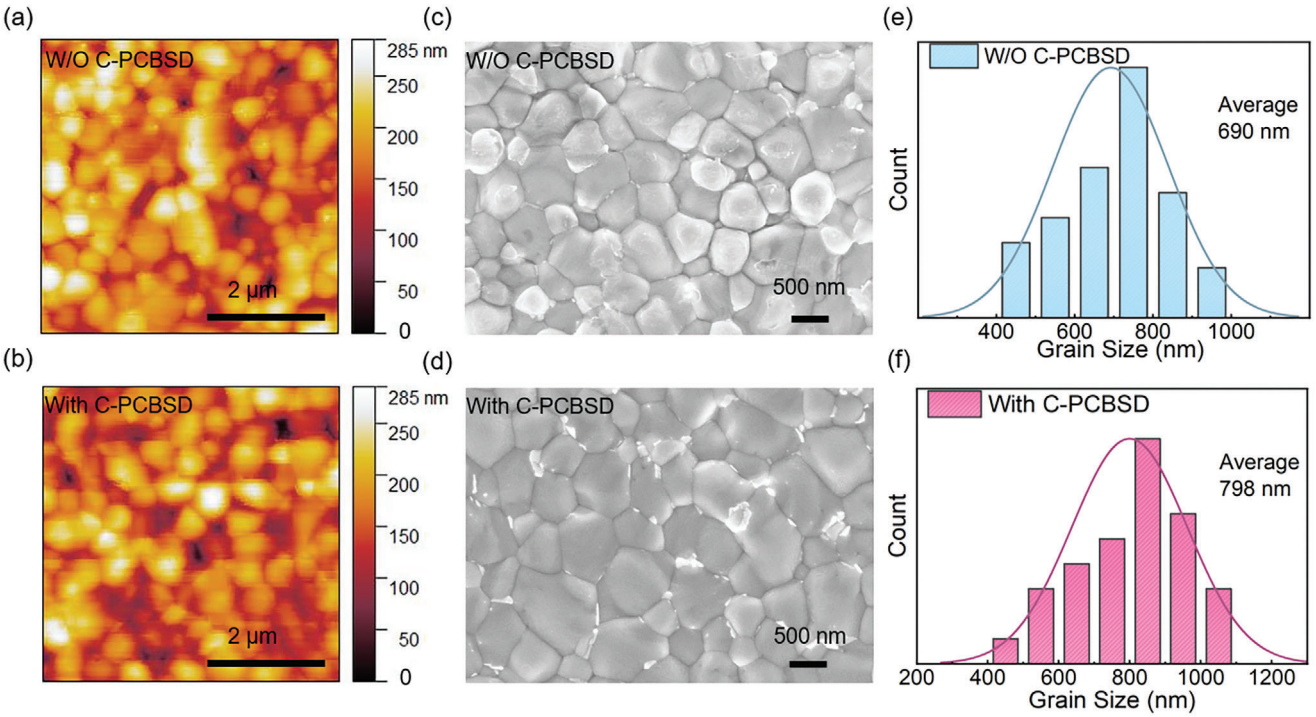

Figure 2. a) AFM images of perovskite films without C-PCBSD and b) with C-PCBSD. c) SEM images of perovskite film without C-PCBSD and d) with C-PCBSD. Grain size histogram of perovskite films based on FTO/PEDOT:PSS/perovskite e) without C-PCBSD and f) with C-PCBSD.

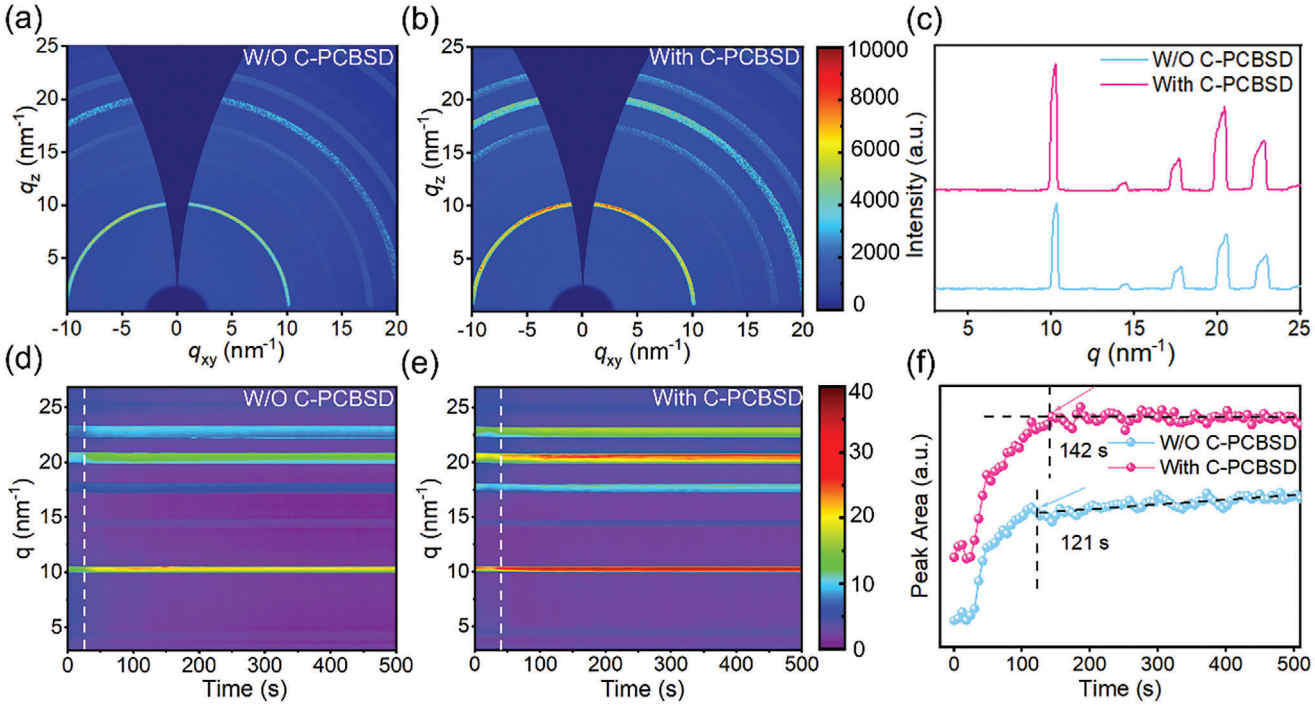

Figure 3. 2D GIWAXS patterns at grazing incidence angle of 0.4 for a) control and b) C-PCBSD-based films. c) 1D GIWAXS azimuthal profiles along the out-of-plane direction for control and C-PCBSD-based films. In situ GIWAXS to analyze the crystallization kinetics of perovskite film. q integral change with time in d) control and e) C-PCBSD-based films. f) Peak area variation with time along with $q = 10$ nm^{-1} for control and C-PCBSD-based films from (a) and (b).

black parts compare to C-PCBSD-based film. The black parts are the lower location in perovskite film surface. Meanwhile, C-PCBSD-treated perovskite films exhibit fewer grain boundaries than the control film. To further investigate the effect of C-PCBSD on the surface morphology of perovskite film, we performed AFM measurements to explore the root-mean-square (RMS) roughness. C-PCBSD-treated perovskite films show a smoother surface (RMS = 10.1), significantly lower than the control film (RMS = 15.6) (Figure S3, Supporting Information). Likewise, the SEM images show a similar surface morphology (Figure 2c,d). The bright objects in Figure 2c,d are most likely PbI_2 from the unreacted precursor material or the degradation product.[26] The C-PCBSD-treated film (800 nm) shows an increased grain size and fewer grain boundaries than the control film (700 nm) (Figure 2e,f). We attribute these phenomena to the thermal cross-linking and the uniform distribution of fullerenes.[27] Meanwhile, we carried out the SEM cross-section measurement, as shown in Figure S4 (Supporting Information). The perovskite film with C-PCBSD shows fewer grain boundaries, decreased surface defect density, and a smoother surface compared to the control film. The SEM cross-section of perovskite films shown the similar result. This result indicates that the interaction between C-PCBSD and perovskite precursors significantly improves the bulk and surface crystallinity of Sn-Pb perovskite thin films.

We used X-ray diffraction (XRD) to investigate the influence of C-PCBSD on the crystalline characteristics of perovskite film. As shown in Figure S5 (Supporting Information), the peak intensity of the C-PCBSD-based film is significantly higher than the control film, which indicates that the C-PCBSD-based surface treatment improves perovskite film crystallinity. We carried out GIWAXS to further investigate the crystallinity of C-PCBSD-modified perovskite films. **Figure** 3a,b shows that the Debye–Scherrer-like ring (D–S ring) intensity at the (100) and (200) crystal planes at $q \approx 10$ nm^{-1} in C-PCBSD-treated film is higher than in the control film. Figure 3c shows the GIWAXS azimuthal profiles along the out-of-plane direction. The results confirm that the C-PCBSD additive enhances peak intensity, attributed to the improvement in the crystallinity of perovskite film.[25] In addition, we carried out the in situ GIWAXS measurements to explore the kinetics of Sn-Pb perovskite films during spin-coating (0–50 s) and annealing process (0–500 s). The antisolvent chlorobenzene, without or with C-PCBSD, was dripped at the 30 s mark as shown in Figure S6 (Supporting Information). The antisolvent dripping ended the initial stage of the perovskite and began the crystallization of Sn-Pb perovskite. The C-PCBSD-based perovskite shows higher intensity and a faster crystallization rate, indicating that it promotes perovskite nucleation and crystal growth. The C-PCBSD perovskite has a longer crystallization time than the control perovskite sample, indicating more complete nucleus growth and higher crystallization of tin-lead perovskite.[28] In addition, Figure 3d,e shows the in situ GIWAXS during annealing process. In the early annealing stage, the C-PCBSD-treated film (0–40 s) shows higher diffraction intensity than the control film (0–26 s). The enhanced diffraction intensity demonstrates that adding C-PCBSD improve the perovskite crystallinity.[29] Moreover, the primary crystal conversion time in C-PCBSD-treated film was extended over 10 s. The crystallization process is retarded,

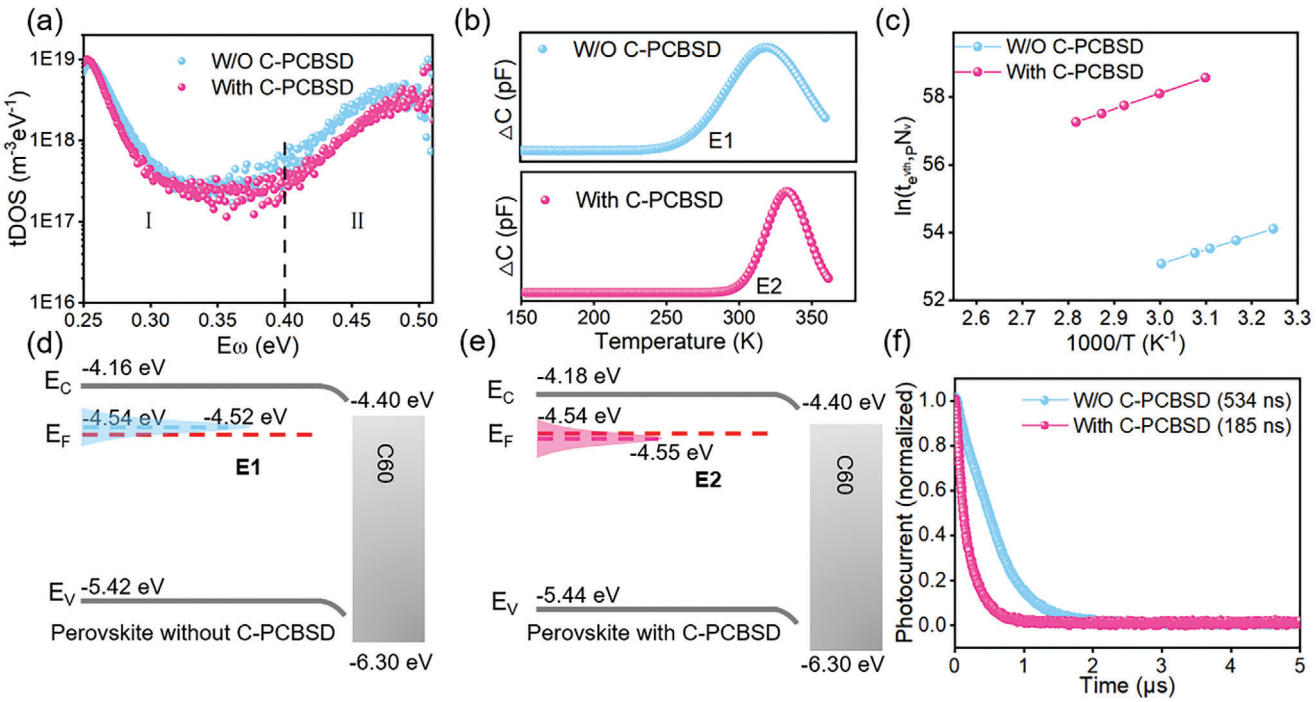

Figure 4. a) tDOS on control and C-PCBSD-treated PSCs. b) DLTS signal from bare perovskite (control, blue) and C-PCBSD-modified PSCs (C-PCBSD, pink). The data points in (b) are obtained by calculating internal transients included in the DLTS signals using the discrete Laplace transform, and the solid lines are linear fits of the data points. c) Arrhenius plots obtained from DLTS signals. Schematic energy level diagram and deep-level traps of d) Control and e) C-PCBSD-modified devices. The peak location and height correspond to the depth and density of E1 and E2 traps. f) Normalized TPC plots of PSCs w/o and with C-PCBSD.

probably influenced by the coordination interaction between C═O groups in C-PCBSD and Sn^{2+} and Pb^{2+} centers. The delayed crystallization induces the formation of more uniformly complete nucleation sites and bigger grains, forming high-quality perovskite films, agreeing with the AFM and SEM results.[30] Figure 3f shows the evolution of peak area of $q = 10$ nm^{-1} in Figure 3d,e with time, which demonstrates the enhanced peak area for C-PCBSD-treated film in comparison with the control one. Moreover, crystallization time increases from 121 to 142 s which proves the addition of C-PCBSD effectively retarded the crystallization process of perovskite.[30] This result indicates that the interaction between C-PCBSD and Sn^{2+} and Pb^{2+} significantly improves the crystallization dynamics of Sn-Pb perovskite thin films.

To explore the effect of the cross-linked C-PCBSD additive on defect properties and carrier recombination behavior in Sn-Pb PSCs, we analyze the energy-dependent trap density of states by thermal admittance spectroscopy (TAS) and deep-level transient spectroscopy (DLTS). **Figure** 4a shows the trap density of state (tDOS). The C-PCBSD-treated device shows a lower trap density than the control device in the shallow-level defect (0.26–0.4 eV) and deep-level defect regions (0.4–0.5 eV). This result indicates the shallow level trap density (Sn vacancy) is decreased.[31] Furthermore, Figure 4b,c shows the effect of C-PCBSD on the deep-level defects of PSCs, where all the devices display the n-type deep-level defects for electron carriers. We extracted these traps' energetic locations and depth (active energy) from the Arrhenius plot using a linear fitting of DLTS peaks (Figure 4c). The control device shows a deep-level trap denoted as E1 (0.360 eV), and the C-PCBSD-based one shows a trap denoted as E2 (0.371 eV), below the conduction band minimum. The C-PCBSD-treated sample shows reduced trap density (2.20×10^{14} cm^{-3}) compared with the control sample (3.22×10^{14} cm^{-3}), as shown in Table S1 (Supporting Information). In addition, the captured cross-section area decreases from 2.47×10^{-18} to 2.30×10^{-20} cm^2, indicating fewer carriers are trapped. The DLTS result demonstrates that the C-PCBSD-based device presents lower surface recombination velocity and longer bulk lifetime.[32,33] Thus, adding C-PCBSD has an effective passivation effect on uncoordinated Pb and Sn defects at the surface and bulk in perovskite. Besides, we carried out UV–vis absorption spectroscopy to investigate the effects of C-PCBSD on the optical absorption of the perovskite film. As shown in Figure S7 (Supporting Information), the bandgap and light absorption of C-PCBSD film barely changed.[34] Ultraviolet photoelectron spectroscopy (UPS) was used to measure the electron energy level structure of perovskite films (Figure S8, Supporting Information); the trap depth and density are shown in Figure 4d,e. The shift of Fermi level energy (E_f) implies that the C-PCBSD-based perovskite surface has a reduced hole concentration. This indicates that the addition of C-PCBSD suppresses the oxidation of Sn^{2+} and reduces carrier accumulation and recombination.[35] We carried out the space charge limited current (SCLC) tests for devices with the hole-only (glass/FTO/PEDOT:PSS/perovskite/PEDOT/Ag) and electron-only structures (glass/FTO/SnO_2/perovskite/C_{60}/Ag). Figure S9 (Supporting Information) shows the filled limit voltage (V_{TFL}) of control and C-PCBSD-based devices are 0.26 and 0.32 V, respectively. Correspondingly, the trap density decreases

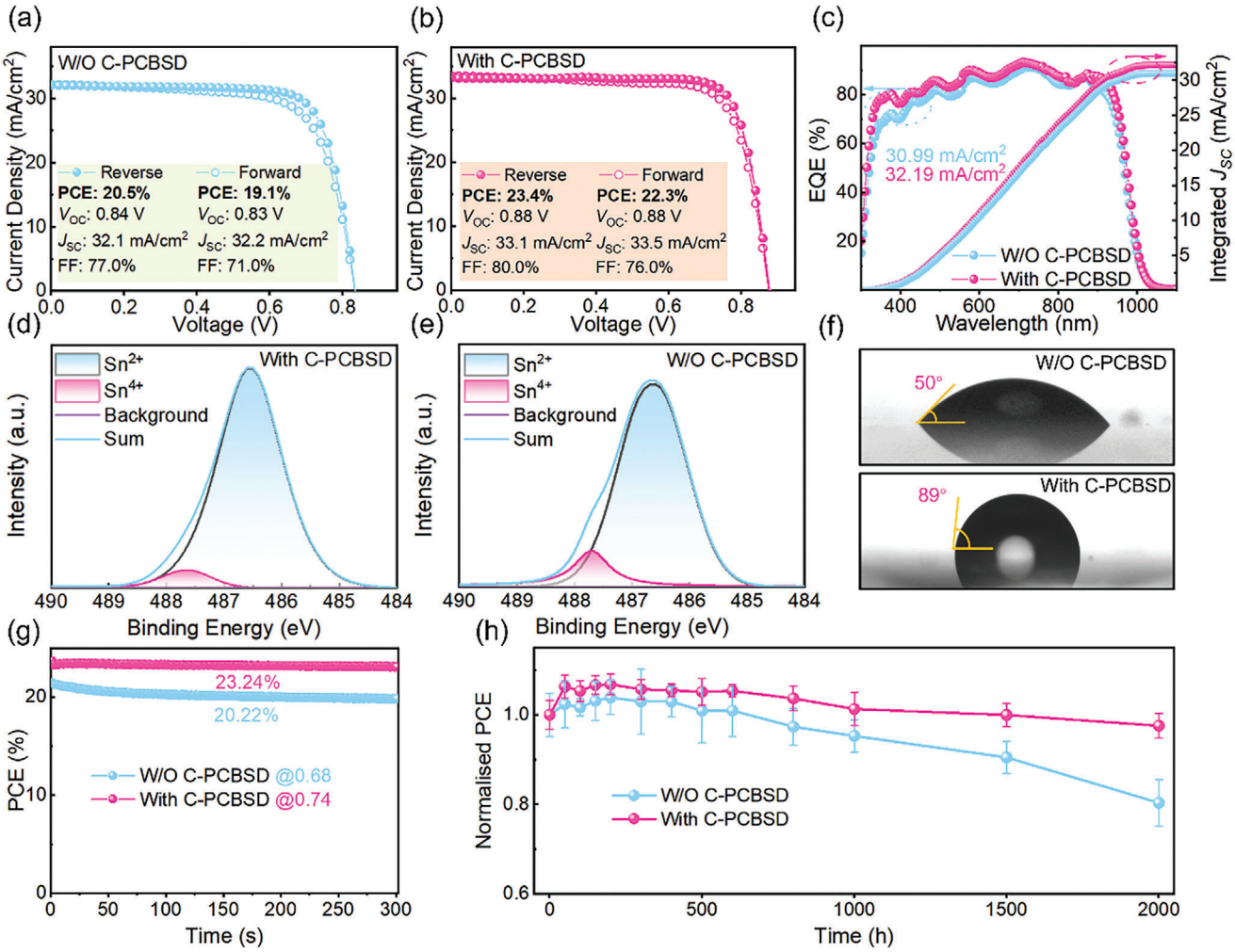

Figure 5. a) *J–V* curves of the control and b) C-PCBSD-based devices. c) EQE spectra and integrated J_{SC} of the PSCs. XPS spectra of Sn element of d) Control and e) C-PCBSD-treated perovskite film. f) Contact angles of water on control and C-PCBSD-treated perovskite films. g) MPPT and h) Shelf-stability in a N_2-filled glovebox for 2000 h of control and PCBSD-based devices.

from 2.71×10^{15} to 2.2×10^{15} cm^{-3}. Meanwhile, compared with the control device, the electron-only structure trap density is decreased from 4.15×10^{15} to 3.38×10^{15} cm^{-3} when treated with C-PCBSD. This result demonstrates the nonradiative recombination caused by interface defects is inhibited.[36–38] Meanwhile, the trap densities both electron-only and hole-only devices are reduced indicating that the bulk defects of perovskite also are suppressed. This result is consistent with DLTS data. Additionally, we performed Mott–Schottky analysis to investigate the influence of cross-linked C-PCBSD on charge behavior, as shown in Figure S10 (Supporting Information). The built-in potential (Vbi) of the C-PCBSD-based device is 0.64 V, compared to 0.61 V for the control device. The higher built-in electric field in the C-PCBSD-based devices indicates more efficient charge extraction and collection.[39]

Dark *J–V* curves and electrochemical impedance spectroscopy (EIS) are used to analyze the carrier recombination behaviors of the PSCs to understand the influence of C-PCBSD on charge carrier dynamics. C-PCBSD devices exhibit lower dark current density than control devices as shown in Figure S11 (Supporting Information). The PSCs based on the C-PCBSD treated exhibit reduced reverse saturation current, which originates from the faster charge transfer and less charge accumulation due to the introduction of C-PCBSD at the surface of perovskite.[40] Figure S12 (Supporting Information) shows electrochemical impedance spectra (EIS). The equivalent circuit includes both series resistance (R_s) and recombination resistance (R_{rec}). The C-PCBSD device exhibits a higher R_{rec} (78 156 Ω) and lower R_s (11.74 Ω) compare to the control device (R_{rec} 24 942 and R_s 15.75 Ω, respectively). These results indicate that adding C-PCBSD can significantly inhibit charge recombination and improve carrier transportation.[41] We also analyzed transient photocurrent (TPC) and transient photovoltage (TPV) decay to investigate the charge transport properties. The time constants for charge collection (τ_C) extracted from the photocurrent decay measurements (TPC) are plotted in Figure 4f. The τ_C values for the control and C-PCBSD-treated devices were 534 and 185 ns, respectively, indicating a facilitated charge carrier collection in the

C-PCBSD-based device.[42–43] Meanwhile, the Transient Photovoltage (TPV) results of the two cells are given in Figure S13 (Supporting Information). The cells without C-PCBSD and with C-PCBSD show a carrier lifetime of 534 and 1023 µs, respectively. A longer carrier lifetime indicates suppressed charge recombination.[44] This could prove that the addition of C-PCBSD can effectively reduce film defects, improve film quality, and inhibit nonradiative recombination. We attribute these results to the coordination ability of C═O moieties in C-PCBSD with Sn vacancies and uncoordinated Pb, which is consistent with the tDOS.

We investigated the effect of C-PCBSD addition on device photovoltaic performance. The *J–V* characteristic curves of photovoltaic devices are obtained under AM1.5G, as shown in **Figure 5a**. It was observed that the control device exhibits a PCE of 20.5%, an open-circuit voltage (V_{OC}) of 0.84 V, a short-circuit current density (J_{SC}) of 32.05 mA cm^{-2}, and an FF of 77%. The optimal concentration of the C-PCBSD-based device is 0.8 mg mL^{-1} (Figure S14, Supporting Information). The C-PCBSD-treated device shows an efficiency of 23.40% with a V_{OC}, J_{SC}, and FF of 0.88 V, 33.16 mA cm^{-2}, and 80%, respectively. The statistical distribution of photovoltaic performance parameters of the devices is shown in Figure S15 (Supporting Information), indicating that the C-PCBSD-treated devices have excellent reproducibility. Figure 5c exhibits the corresponding external quantum efficiency (EQE) and integrated J_{SC} of the control and C-PCBSD-treated devices. The integrated J_{SC} values of the C-PCBSD-treated and control devices are 32.19 and 30.99 mA cm^{-2}, respectively. It is consistent with the results obtained from the *J–V* curve. The photovoltaic performance improvement in devices originates from enhancements of V_{OC} and FF. We attributed the coordination interactions between C═O of C-PCBSD and Sn vacancies and uncoordinated Pb of perovskite. These results can reduce defect-assist nonradiative recombination, improve interface contact and bulk crystallinity.[45–47] Besides, we investigate the water and oxygen resistance effects of C-PCBSD on perovskite devices. Figure 5d,e; and Figure S16 (Supporting Information) exhibit the Sn^{4+}/Sn ratio of perovskite films exposed to ambient air with RH of ≈60%–80% at 5, 30, and 120 min. The ratio of Sn^{4+}/Sn of C-PCBSD-treated film (9.54%) is lower than the control film (12.76%). With the time increasing, we find that the Sn^{4+}/Sn ratio of the C-PCBSD-based film (30 min: 9.55%, 120 min: 10.26%) is still lower than the control film (30 min: 15.22%, 120 min: 29.34%). In addition, we carried out contact angle measurements to investigate the hydrophobicity of the prepared films. Figure 5f; and Figure S17 (Supporting Information) exhibit the contact angle of water drops on perovskite films exposed to air with RH of ≈60%–80% for different times (0, 2, and 6 h). The C-PCBSD-treated film shows a larger water contact angle (0 h: 89°, 2 h: 87°, 6 h: 86°) than the control film (0 h: 50°, 2 h: 44°, 6 h: 40°). These results indicate that the C-PCBSD forms a cross-linked network and coordination to Sn^{2+} from C═O groups that effectively improve resistance to oxidation and hydrophobicity.

To further study the long-term water and oxygen resistance stability of C-PCBSD on perovskite devices, Figure S18 (Supporting Information) shows the long-term stability of devices exposed to ambient air with RH of ≈30%–40% for 10 min per day. The C-PCBSD-treated device maintains around 96% of its initial efficiency after 1000 h. We also measure the power outputs with photocurrent and efficiency under maximum power points tracking (MPPT) at AM1.5G condition, which evidence the better performance of C-PCBSD-based device compared to the control one, as shown in Figure 5g. We further investigate the effect of C-PCBSD on the long-term stability of unencapsulated perovskite devices in a N_2-filled glovebox at room temperature (≈25 °C). Figure 5h shows that adding C-PCBSD perovskite devices exhibits enhanced stability, and the efficiency remains at 97% after 2000 h. However, the control device retains only 80% of its initial efficiency after 2000 h. Thus, C-PCBSD-based devices exhibit improved material and device stability compared to control devices, in-operando and under storage in different atmospheric conditions, proving overall the higher robustness achieved after C-PCBSD modification.

3. Conclusion

In summary, we present the successful antisolvent engineering of mixed Sn-Pb perovskites with a thermally cross-linked network. The coordination ability of C═O groups in C-PCBSD modifier with Sn^{2+} and Pb^{2+} retards the crystallization process, suppresses the oxidation of Sn^{2+}, improves the perovskite crystallinity, and decreases the surface trap density, greatly improving charge extraction at the interface. Consequently, the modified devices with the synergistic effect of C-PCBSD obtaining a champion PCE of 23.4% with improved V_{OC} and FF. Subsequently, the cross-linked polymerization network formed on the perovskite surface prevents the invasion of water and oxygen. Thus, the devices with C-PCBSD maintain 96% of their initial efficiency in an outdoor atmosphere exposed for 10 min day^{-1} after 1000 h. Besides, the devices kept 97% of their initial PCE in N_2 atmosphere after 2000 h. This work highlights the potential of cross-linkable perovskite-capping networks as effective antisolvent engineering for further advancing the fabrication of efficient and stable mixed Sn-Pb PSCs.

Supporting Information

Supporting Information is available from the Wiley Online Library or from the author.

Acknowledgements

Z.J. and Z.S. contributed equally to this work. The authors thanked the beamlines BL14B1 and BL03HB at the Shanghai Synchrotron Radiation Facility for providing the beam time. The authors acknowledged the support of the Joint Fund of Provincial Science and Technology Research and Development plan of Henan Province (No. 232301420004), and the Outstanding Youth Fund of the Natural Science Foundation of Henan Province (No. 242300421069). Z.L. acknowledged the financial support from the AXA research fund.

Conflict of Interest

The authors declare no conflict of interest.

Data Availability Statement

Research data are not shared.

Keywords

cross-link fullerene, defect passivation, long time stability, Sn-Pb perovskite solar cell

Received: May 1, 2024
Revised: July 5, 2024
Published online: July 20, 2024

[1] D. W. de Quilettes, S. M. Vorpahl, S. D. Stranks, H. Nagaoka, G. E. Eperon, M. E. Ziffer, H. J. Snaith, D. S. Ginger, *Science* **2015**, *348*, 683.
[2] S. D. Stranks, G. E. Eperon, G. Grancini, C. Menelaou, M. J. Alcocer, T. Leijtens, L. M. Herz, A. Petrozza, H. J. Snaith, *Science* **2013**, *342*, 341.
[3] I. Chung, B. Lee, J. He, R. P. Chang, M. G. Kanatzidis, *Nature* **2012**, *485*, 486.
[4] G. Li, Z. Su, L. Canil, D. Hughes, M. H. Aldamasy, J. Dagar, S. Trofimov, L. Wang, W. Zuo, J. J. Jerónimo-Rendon, *Science* **2023**, *379*, 399.
[5] H. Chen, C. Liu, J. Xu, A. Maxwell, W. Zhou, Y. Yang, Q. Zhou, A. S. Bati, H. Wan, Z. Wang, *Science* **2024**, *384*, 189.
[6] G. Wu, R. Liang, M. Ge, G. Sun, Y. Zhang, G. Xing, *Adv. Mater.* **2022**, *34*, 2105635.
[7] Z. Ni, C. Bao, Y. Liu, Q. Jiang, W.-Q. Wu, S. Chen, X. Dai, B. Chen, B. Hartweg, Z. Yu, Z. Holman, J. Huang, *Science* **2020**, *367*, 1352.
[8] R. Lin, J. Xu, M. Wei, Y. Wang, Z. Qin, Z. Liu, J. Wu, K. Xiao, B. Chen, S. M. Park, *Nature* **2022**, *603*, 73.
[9] K. J. Savill, A. M. Ulatowski, L. M. Herz, *ACS Energy Lett.* **2021**, *6*, 2413.
[10] X. Li, X. Wu, B. Li, Z. Cen, Y. Shang, W. Lian, R. Cao, L. Jia, Z. Li, D. Gao, *Energy Environ. Sci.* **2022**, *15*, 4813.
[11] D. Luo, R. Su, W. Zhang, Q. Gong, R. Zhu, *Nat. Rev. Mater.* **2020**, *5*, 44.
[12] J. Wang, J. Zhang, Y. Zhou, H. Liu, Q. Xue, X. Li, C.-C. Chueh, H.-L. Yip, Z. Zhu, A. K. Jen, *Nat. Commun.* **2020**, *11*, 177.
[13] J. Zhao, Z. Zhang, G. Li, M. H. Aldamasy, M. Li, A. Abate, *Adv. Energy Mater.* **2023**, *13*, 2204233.
[14] H. Liu, Z. Zhang, W. Zuo, R. Roy, M. Li, M. M. Byranvand, M. Saliba, *Adv. Energy Mater.* **2023**, *13*, 2202209.
[15] Z. Zhang, L. Qiao, K. Meng, R. Long, G. Chen, P. Gao, *Chem. Soc. Rev.* **2023**, *52*, 163.
[16] C. Tian, Z. Zhang, A. Sun, J. Liang, Y. Zheng, X. Wu, Y. Liu, C. Tang, C.-C. Chen, *Nano Energy* **2023**, *116*, 108848.
[17] J. Tang, L. Liu, Z. Yu, J. Du, X. Cai, M. Zhang, M. Zhao, L. Bai, Z. Gai, S. Cui, *Adv. Sustainable Syst.* **2022**, *6*, 2100510.
[18] J. Warby, F. Zu, S. Zeiske, E. Gutierrez-Partida, L. Frohloff, S. Kahmann, K. Frohna, E. Mosconi, E. Radicchi, F. Lang, *Adv. Energy Mater.* **2022**, *12*, 2103567.
[19] B. Li, X. Wu, H. Zhang, S. Zhang, Z. Li, D. Gao, C. Zhang, M. Chen, S. Xiao, A. K. Y. Jen, *Adv. Funct. Mater.* **2022**, *32*, 2205870.
[20] M.-W. An, Z. Xing, B.-S. Wu, F.-F. Xie, S.-Y. Zheng, L.-L. Deng, X. Wang, B.-W. Chen, D.-Q. Yun, S.-Y. Xie, *Rare Met.* **2021**, *40*, 1691.
[21] C. Tao, J. Van Der Velden, L. Cabau, N. F. Montcada, S. Neutzner, A. R. Srimath Kandada, S. Marras, L. Brambilla, M. Tommasini, W. Xu, *Adv. Mater.* **2017**, *29*, 1604493.
[22] F. Wu, T. Chen, X. Yue, L. Zhu, *Org. Electron.* **2018**, *58*, 6.
[23] T. Wang, W. Deng, J. Cao, F. Yan, *Adv. Energy Mater.* **2023**, *13*, 2201436.
[24] Z. Wu, S. R. Raga, E. J. Juarez-Perez, X. Yao, Y. Jiang, L. K. Ono, Z. Ning, H. Tian, Y. Qi, *Adv. Mater.* **2018**, *30*, 1703670.
[25] M. Li, Y.-H. Chao, T. Kang, Z.-K. Wang, Y.-G. Yang, S.-L. Feng, Y. Hu, X.-Y. Gao, L.-S. Liao, C.-S. Hsu, *J. Mater. Chem. A* **2016**, *4*, 15088.
[26] S. Hu, K. Otsuka, R. Murdey, T. Nakamura, M. A. Truong, T. Yamada, T. Handa, K. Matsuda, K. Nakano, A. Sato, *Energy Environ. Sci.* **2022**, *15*, 2096.
[27] M. Li, Z.-K. Wang, T. Kang, Y. Yang, X. Gao, C.-S. Hsu, Y. Li, L.-S. Liao, *Nano Energy* **2018**, *43*, 47.
[28] M. Qin, Y. Li, Y. Yang, P. F. Chan, S. Li, Z. Qin, X. Guo, L. Shu, Y. Zhu, Z. Fan, *ACS Energy Lett.* **2022**, *7*, 3251.
[29] X. Wang, X. Ran, X. Liu, H. Gu, S. Zuo, W. Hui, H. Lu, B. Sun, X. Gao, J. Zhang, *Angew. Chem., Int. Ed.* **2020**, *59*, 13354.
[30] G. Li, Z. Su, M. Li, F. Yang, M. H. Aldamasy, J. Pascual, F. Yang, H. Liu, W. Zuo, D. Di Girolamo, *Adv. Energy Mater.* **2021**, *11*, 2101539.
[31] X. Zheng, B. Chen, J. Dai, Y. Fang, Y. Bai, Y. Lin, H. Wei, X. C. Zeng, J. Huang, *Nat. Energy* **2017**, *2*, 1.
[32] Z. Zhu, K. Mao, K. Zhang, W. Peng, J. Zhang, H. Meng, S. Cheng, T. Li, H. Lin, Q. Chen, *Joule* **2022**, *6*, 2849.
[33] H. Meng, K. Mao, F. Cai, K. Zhang, S. Yuan, T. Li, F. Cao, Z. Su, Z. Zhu, X. Feng, *Nat. Energy* **2024**, *9*, 536.
[34] J. Yang, S. Xiong, J. Song, H. Wu, Y. Zeng, L. Lu, K. Shen, T. Hao, Z. Ma, F. Liu, *Adv. Energy Mater.* **2020**, *10*, 2000687.
[35] J. Luo, R. He, H. Lai, C. Chen, J. Zhu, Y. Xu, F. Yao, T. Ma, Y. Luo, Z. Yi, *Adv. Mater.* **2023**, *35*, 2300352.
[36] Y. Shao, Z. Xiao, C. Bi, Y. Yuan, J. Huang, *Nat. Commun.* **2014**, *5*, 5784.
[37] M. J. Trimpl, A. D. Wright, K. Schutt, L. R. Buizza, Z. Wang, M. B. Johnston, H. J. Snaith, P. Müller-Buschbaum, L. M. Herz, *Adv. Funct. Mater.* **2020**, *30*, 2004312.
[38] B. Li, K. Yang, Q. Liao, Y. Wang, M. Su, Y. Li, Y. Shi, X. Feng, J. Huang, H. Sun, *Adv. Funct. Mater.* **2021**, *31*, 2100332.
[39] L. Qiao, T. Ye, P. Wang, T. Wang, L. Zhang, R. Sun, W. Kong, X. Yang, *Adv. Funct. Mater.* **2024**, *34*, 2308908.
[40] J. Zhang, B. Yu, Y. Sun, H. Yu, *Adv. Energy Mater.* **2023**, *13*, 2300382.
[41] C. Xu, S. Zhang, W. Fan, F. Cheng, H. Sun, Z. Kang, Y. Zhang, *Adv. Mater.* **2023**, *35*, 2207172.
[42] M. Wang, S. Tan, Y. Zhao, P. Zhu, Y. Yin, Y. Feng, T. Huang, J. Xue, R. Wang, G. S. Han, *Adv. Funct. Mater.* **2021**, *31*, 2007520.
[43] C. Qiu, L. Wagner, J. Liu, W. Zhang, J. Du, Q. Wang, Y. Hu, H. Han, *EcoMat* **2023**, *5*, e12268.
[44] Y. Chang, X. Zhu, Y. Shi, Y. Liu, K. Meng, Y. Li, J. Xue, L. Zhu, J. Zhang, H. Zhou, *Energy Environ. Sci.* **2022**, *15*, 2937.
[45] K.-W. Yeom, D.-K. Lee, N.-G. Park, *Adv. Energy Mater.* **2022**, *12*, 2202496.
[46] W. Ke, C. Xiao, C. Wang, B. Saparov, H.-S. Duan, D. Zhao, Z. Xiao, P. Schulz, S. P. Harvey, W. Liao, *Adv. Mater.* **2016**, 28.
[47] J. Zhang, Z. Li, F. Guo, H. Jiang, W. Yan, C. Peng, R. Liu, L. Wang, H. Gao, S. Pang, *Angew. Chem., Int. Ed.* **2023**, *135*, 202305221.